

Article

Design Optimization and Analysis of an Outer-Rotor Direct-Drive Permanent-Magnet Motor for Medium-Speed Electric Vehicle

Yuan Yuan ^{1,*}, Wenjun Meng ¹, Xiaoxia Sun ¹ and Liyong Zhang ²

¹ School of Mechanical Engineering, Taiyuan University of Science and Technology, Taiyuan 030024, China; 1984018@tyust.edu.cn (W.M.); xiaoxiasun@tyust.edu.cn (X.S.)

² Great Wall Motor Company Limited, Baoding 071000, China; tyustzly@163.com

* Correspondence: yuanyuan525622@126.com

Received: 18 February 2019; Accepted: 20 March 2019; Published: 4 April 2019

Abstract: At present, it is the conventional inner rotor motor instead of the internal combustion engine that is adopted by most electric cars. However, compared to the traditional centralized driving pattern, cars adopting a distributed direct driving pattern have higher drive efficiency and more stable handling. Given this background, a kind of direct-drive outer rotor motor with 40 poles and 42 slots applied for middle or low speed electric cars was designed. The core of this study included the electromagnetic analysis and structural design of the motor. Firstly, the material and dimension parameters of the stator and rotor were selected and calculated by the traditional method. The air-gap length and pole-arc coefficient were optimized using an RMxpert module, which was developed using the equivalent magnetic circuit method. Then, a two-dimensional finite-element model was established using ANSYS Maxwell. The magnetic field and torque characteristics of the model were then analyzed. Results show that the design of the motor is reasonable. In addition, a method for reducing the torque ripple was proposed and verified by simulation.

Keywords: outer rotor; direct-drive brushless DC motor; structural design; electromagnetic analysis; torque ripple

1. Introduction

In the development of the modern industrial rise today, the automotive industry has become a “bright pearl” of the tech world. However, with the development of the automobile industry, energy is consumed, and steadily each year more than 60% of the world’s oil resources are consumed by the auto industry [1]. The development of new energy vehicles has become the hotspot of research. In new energy vehicles, electric vehicles have become a mainstay in the new energy vehicles because of their minimal pollution of the environment, low energy consumption, flexible control, and some other advantages. Electric vehicles are listed in China’s 13th five-year plan and have become a key research area of the made in China 2025 program; their future development space is enormous [2,3].

There are two driving methods for electric vehicles, which are divided into centralized single motor drive and distributed multi-motor drive [4]. In roughly the same driving mode, the centralized driving electric vehicle is comparable with the conventional internal combustion engine vehicle. The engine or the electric motor is used as the driving mechanism, and the transmission and the transmission shaft are used as the transmission mechanism. Thus, the centralized driving system occupies a large volume, which result in a small utility space for the vehicle, the energy loss is high, and energy utilization efficiency is low. Compared with the centralized drive, the distributed drive eliminates the intermediate transmission mechanism and places the motor directly in the drive wheel, saving the space occupied by the engine and reducing the mass of the whole vehicle. At the same

time, the regenerative technology of energy braking can be used. The energy in braking and downhill conditions is recycled and utilized to increase the mileage of electric vehicles [5]. Distributed drives can be divided into two types: deceleration drive and direct drive [6]. The deceleration driving method drives the motor by integrating the motor and the speed reducer with a certain reduction ratio. The technology is relatively simple but widely used, and the wheel drive method adopted by the leader of electric vehicles, Tesla automobiles [7]. The direct drive mode directly drives the car with a low-speed permanent-magnet motor. The permanent-magnet motor is generally an outer rotor type. This type of drive can not only flexibly arrange the drive but can also realize the individual control of multiple wheels of the car, as well as vehicle dynamics control technology, such as electronic stability program (ESP), anti-lock brake system (ABS), and electronic brakeforce distribution (EBD) [8].

In 2007, the team led by S. Ekram [9] optimized the cogging torque and increased torque to design a permanent-magnet brushless outer rotor motor that was designed with air gap length, cogging width, and winding turns. In the variable, multi-objective optimization design, the subsequent experimental comparison shows that the cogging torque fluctuation is obviously suppressed, and the radial unbalance force is also reduced by 24%, achieving the purpose of optimization. In 2010, Gombert et al. [10] designed a 17-inch hub motor, which could directly replace the hub in the city tram. The experimental results showed that the efficiency of the motor gradually increased as the speed increased, with the peak efficiency up to 94%, satisfying the standards of passenger vehicles. In 2012, Arnold J. Rix [11] studied the effect of different stator and rotor structures on the performance of the hub motor. By comparing different stator and stator pairs of motors, it was found that the influence of different pole pairs on winding loss was closely related to the motor speed; the higher the speed, the more obvious the difference. In 2012, K. Emmrich [12] led the team to study the influence of temperature on the electric wheel drive system. The transient thermal simulation of the motor was carried out. The results showed that the temperature was the main influencing factor on the motor performance. If the temperature exceeded a certain value, magnetic steel demagnetization would threaten driving safety. In 2013, Chukwuma Junior [13] designed a new type of hub motor. This motor combines the controller inside the motor and divides a controller into eight parts to coordinate the control of the motor, improving the control accuracy and making the motor more reliable. In 2014, Msaddek Hejra et al. [14] designed and optimized a small permanent-magnet hub motor for vehicles. After optimization, it reduced the quality by 20% and optimized the efficiency by 3.7% and supervised the design of permanent-magnet outer rotor motors. Theoretical guidance was given by A. Kock et al. [15] and Tashakori et al. [16], who both studied the fault tolerance of hub motors, and designed the hub motor drive system to compensate the brake torque when the motor failed. This design method not only increased the installation space but also suppressed the torque ripple, and the bench test of the redesigned hub motor proved the rationality of its design.

In this study, an outer-rotor brushless DC motor, which can directly drive the electric vehicle, was designed. It deviates from the structure of the traditional electric vehicle drive system. The static and transient magnetic fields of the motor were analyzed comprehensively to verify the rationality of the design. The causes of the torque ripple of the brushless DC motor was analyzed extensively, and the main factor causing the torque ripple was discovered. A segmented stator method was developed to reduce the torque ripple. This method was validated and proved effective by finite-element simulation and harmonic analysis.

2. Design of the Outer-Rotor Direct-Drive Brushless DC Motor

2.1. Design Parameters of the Motor

Taking a certain model of a Geely automobile as the research object, a middle or low speed direct-drive brushless DC motor with an outer-rotor structure was developed. The design parameters of the Geely automobile are presented in Table 1.

Table 1. Parameters of a Geely automobile.

| A Geely Automobile | Technical Parameters | Value |
|--------------------|---|-------|
| Basic parameters | The entire vehicle mass m (kg) | 800 |
| | Windward area A (m^2) | 2 |
| | Coefficient of air resistance C_D | 0.32 |
| | Rolling resistance coefficient f | 0.015 |
| | System transmission efficiency η_r | 0.96 |
| Performance index | The wheel radius r (m) | 0.27 |
| | The maximum speed u_{\max} (km/h) | 80 |
| | The maximum gradeability a ($^\circ$) | 11.3 |
| | 0–60 km/h acceleration time t_a (s) | 9 |

2.1.1. Determination of Motor Power

The minimum power required by the vehicle according to different working conditions can be calculated.

When the car achieves the highest speed, the maximum power of the motor is p_e , the maximum power of the vehicle achieving the maximum gradient is p_a , and the power of the vehicle achieving the highest acceleration time is p_c .

1. Taking the maximum speed as the basis

$$p_e = \frac{u_{\max}}{3600\eta_r} \left(mgf + \frac{C_D A u_{\max}^2}{21.15} \right) \quad (1)$$

2. Taking the climbing capability as the basis

$$p_a = \frac{u_i}{3600\eta_r} \left(mgf \cos \alpha_{\max} + mg \sin \alpha_{\max} + \frac{C_D A u_i^2}{21.15} \right) \quad (2)$$

3. Taking the acceleration capability as the basis

$$p_c = \frac{1}{3600t_a\eta_r} \left(\delta m \frac{u_a^2}{2\sqrt{t_a}} + mgf \frac{u_a}{1.5t_a} + \frac{C_D A u_a^3}{21.15 \times 2.5 t_a} \right) \quad (3)$$

where u_a is the acceleration final velocity(km/h), and δ is the mass conversion coefficient whose value is 1.04.

Furthermore, the motor's power is deduced as

$$p \geq \max[p_e, p_a, p_c] \quad (4)$$

2.1.2. Determination of the Rated Speed and Peak Speed

The design is based on the maximum speed of 80 km/h. Due to the use of an outer-rotor structure, the motor speed is equal to the wheel speed; the maximum speed n_{\max} of the motor is deduced as

$$n_{\max} \geq \frac{u_{\max} \times 10^3}{120\pi r} \quad (5)$$

The relationship between the rated speed and the maximum speed of the motor is deduced as

$$n_{\max} = \beta n_N \quad (6)$$

where β is the expanded constant power meter coefficient; the larger the β is, the greater the output torque of the motor will be, and the better the acceleration and climbing performance of the electric vehicle will be. However, if it is too large, the size of the power converter is large accordingly. Comprehensively, its range is 2 to 4.

According to the above formula, all parameters can be substituted to calculate the design parameters of the brushless DC motor, such as torque, power, and speed, as shown in Table 2.

Table 2. Design requirements of the brushless DC motor.

| Parameters | Value |
|---------------------------|-------------------------|
| Rated power | $p_N = 22kw$ |
| Peak power | $p_{max} = 55kw$ |
| Rated speed | $n_N = 260 r/min$ |
| Maximum speed | $n_{max} = 780 r/min$ |
| Rated torque | $T_N = 2.02 kN \cdot m$ |
| Phase number | $M = 3$ |
| Efficiency | $\eta \geq 85\%$ |
| Permanent magnet material | N35SH |

2.2. Main Dimensions of the Motor and Electromagnetic Load

The main dimensions of the motor include the diameter of the armature and the effective length of the armature core. In addition, the energy conversion process of the motor is completed in the air gap; thus, the air-gap length can be considered the third main dimension of the motor [17]. The calculation and optimization of the main dimensions is a crucial step in the process of motor design.

The electromagnetic load comprises the electrical load A and magnetic load B_δ of the motor, which are closely related to the main dimensions of the motor. These loads exert a significant influence on the mechanical characteristics, efficiency, torque, and other performance parameters of the motor. The relation between the main dimensions of the motor and the electromagnetic load is deduced as

$$D_a^2 L_a = \frac{6.1 \times 10^7}{\alpha_p A B_\delta} \cdot \frac{P_{em}}{n_N} \quad (7)$$

where D_a is the armature diameter (cm), L_a is the length of the stator core (cm), α_p is the pole-arc coefficient whose initial value is 0.7, A is the electrical load set to 300 A/cm in this study, and B_δ is the magnetic load set to 0.96 T.

Substituting the given parameters into Equation (7) yields $D_a^2 L_a = 67844.78 \text{cm}^3$.

The outer rotor will distort under stress given that the electric vehicle drive system is replaced by the outer-rotor direct-drive permanent-magnet brushless DC motor. Setting the dimension of the air-gap inappropriately small may induce friction between the outer rotor and the stator. This outcome should be avoided. Therefore, the air-gap dimension should be sufficiently large. In this study, its initial value is set to 1 mm.

2.3. Design of the Stator and Rotor of the Motor

2.3.1. Dimensions of the Stator and Rotor

Based on an appointed car, the outer diameter of the motor rotor is set to 500 mm. The stability of the running electric vehicle is directly affected when the outer-rotor motor distorts under tension. Thus, the thickness of the rotor core of the motor should be increased, and its initial value is set to 12 mm in this design. The inner diameter of the outer rotor, including the permanent magnet, can be calculated by Equation (8). The outer diameter of the stator can be obtained by subtracting the air-

gap dimension twice, such that the armature diameter is 462 mm, which is then substituted into $D_a^2 L_a = 67844.78 \text{ cm}^3$ to obtain $L_a = 317.86 \text{ mm}$.

$$D_{Ri} = D_{Ro} - 2(h_m + h_R) \quad (8)$$

where D_{Ri} is inner diameter of the outer rotor, D_{Ro} is the outer diameter of the outer rotor, h_m is the thickness of the permanent magnet ($h_m = 6 \text{ mm}$), and h_R is the thickness of rotor core.

2.3.2. Determination of the Armature Winding

The pole number should be increased when the brushless DC motor runs at a middle or low speed. The pole number is set to 40 on the basis of the rated speed of the motor. If the integral-slot winding is adopted, then the tooth-slot number of the three-phase brushless DC motor should be at least at 120. Fractional-slot winding is more suitable given the outer diameter of the motor. The fractional-slot winding structure can significantly reduce not only the tooth-slot number but also the cogging torque. The connection diagram of the three-phase winding of the motor is illustrated in Figure 1.

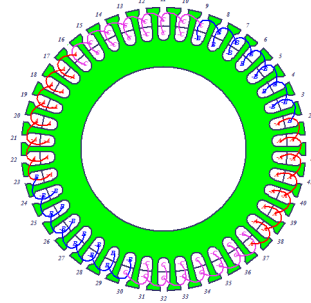


Figure 1. Connection diagram of three-phase windings.

2.3.3. Parameter Optimization Based on the Equivalent Magnetic Circuit Method

After the dimension and material parameters of the motor are determined, the initial parameters should be optimized by magnetic circuit calculation. The magnetic circuit calculation software RMxpert, which is based on the equivalent magnetic circuit method, can directly import the analysis data into ANSYS Maxwell to generate a 2D or 3D motor model [18]. Therefore, optimizing the key parameters of the motor using RMxpert software lays the foundation for the subsequent finite-element simulation of the motor magnetic field and performance analysis.

Optimization of the Air-Gap Length

As mentioned in Section 2.2, the air-gap length can be considered the third main dimension of the motor, and its value exerts a significant influence on the performance of the brushless DC motor. On the condition that the dimensions of the other parameters of the motor are invariable, the air-gap length is optimized by varying its value from 1 mm to 4 mm at a step length of 0.02 mm. The curves of motor efficiency and torque with respect to the air-gap length are presented in Figures 2 and 3, respectively.

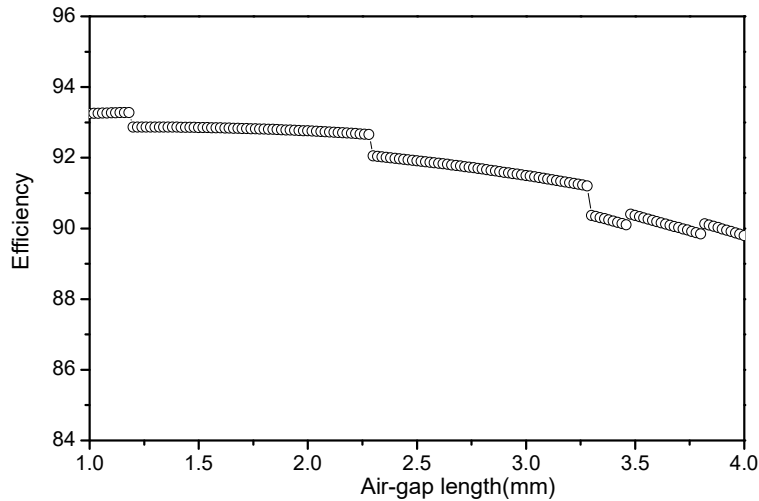


Figure 2. Relation curve between air-gap length and efficiency.

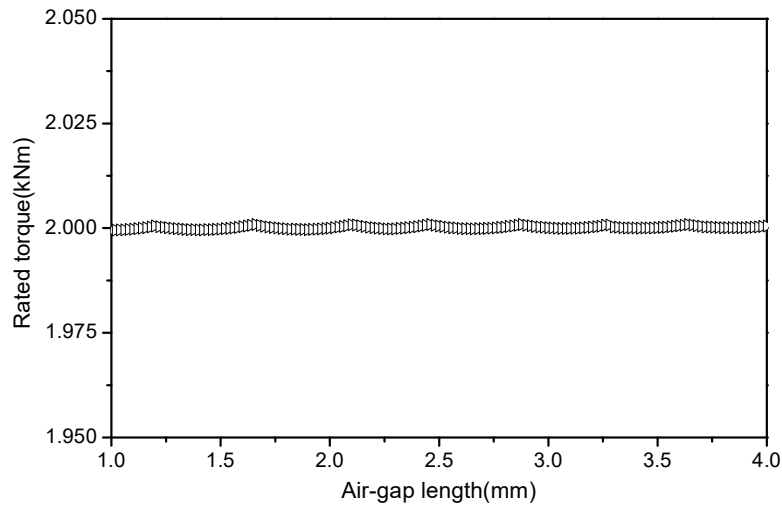


Figure 3. Relation curve between air-gap length and rated torque.

In consideration of the efficiency and torque of the motor as well as the practical application of the design motor, the air-gap length should be increased to 2 mm, which not only guarantees the efficiency of the motor but also improves the running reliability of the motor. Consequently, the excessive deformation of the outer-rotor motor under stress, the friction between the outer rotor and the stator, and the further damage to the motor can be prevented.

Optimization of the Pole-Arc Coefficient

The pole-arc coefficient has considerable influence on the air-gap magnetic flux density, cogging torque, and armature current. For its optimization, the pole-arc coefficient is varied from 0.6 to 0.75 at a step length of 0.02. The air-gap magnetic flux density, cogging torque, and armature average current curves along with the changes in the pole-arc coefficient are obtained by parametric scanning calculation and shown in Figures 4–6, respectively.

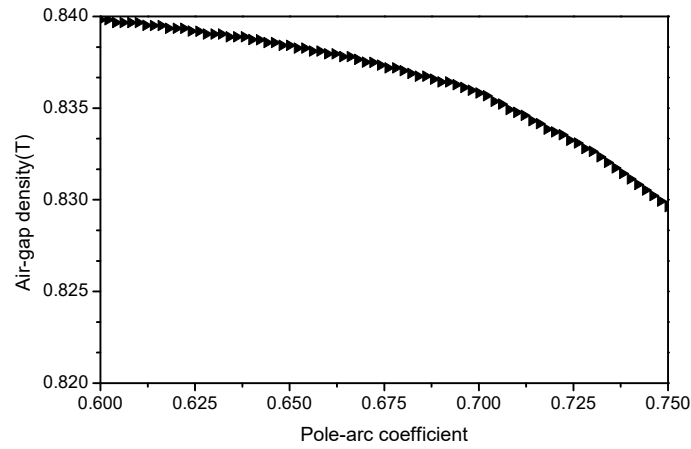


Figure 4. Relation curve between pole-arc coefficient and air-gap density.

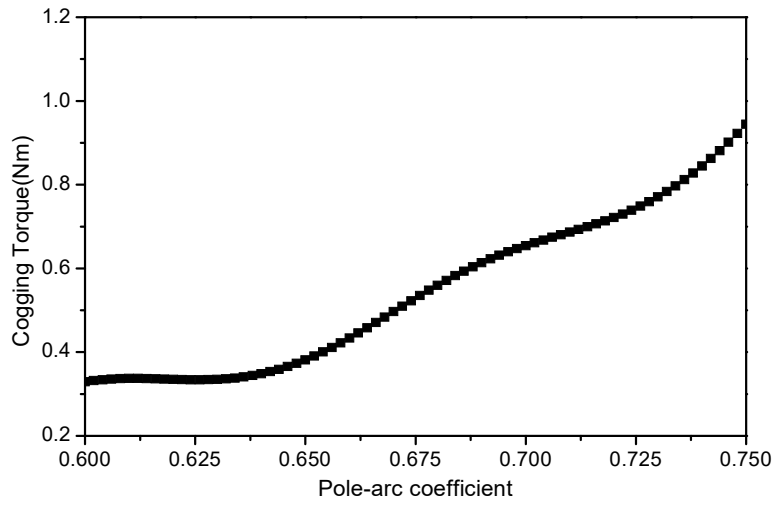


Figure 5. Relation curve between pole-arc coefficient and cogging torque.

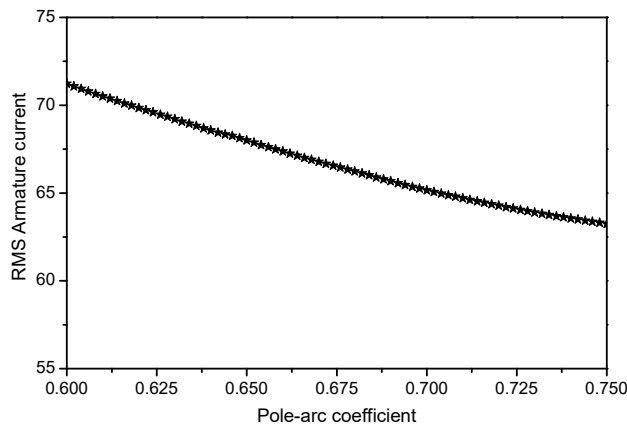


Figure 6. Relation curve between pole-arc coefficient and armature current.

The air-gap flux density should not be excessively low to obtain high torque under low-speed and direct-drive load conditions. Otherwise, high torque will not be achieved. As shown in Figure 4, the pole-arc coefficient should be small. Figure 5 shows that a smaller pole-arc coefficient results in

smaller cogging torque, less torque fluctuation, and better running stability. However, the armature winding current is already high when the motor is running under low-speed high-torque conditions. Figure 6 shows that the armature winding current increases, and permanent-magnet demagnetization is enhanced if the pole-arc coefficient takes a smaller value. As a result, the overheating problem of the motor becomes more severe, and the performance of the permanent magnet is affected, easily leading to permanent demagnetization and permanent damage to the rotor magnetic pole. On the basis of the possible outcomes and the three generated curves, the pole-arc coefficient is adjusted to 0.675, which not only guarantees an increase in the motor magnetic flux density and a decrease in the cogging torque to a certain extent but also ensures that the average current of the armature winding does not excessively increase.

2.3.4. Structural Design of the Motor Stator and Rotor

The structure of the brushless DC motor is designed using the optimized parameters. The motor structure includes the mechanical structures of the stator, rotor, wheel hub, and fixed axis.

Mechanical Structure of the Stator

The dimensions of the low-speed brushless DC motor are larger than an ordinary motor; thus, if the traditional manufacturing method is adopted, then the original manufacturing tools should be upgraded, and the production costs will increase. The coil pitch of the motor is only one, that is, the coil span is a stator tooth when the fractional-slot concentrated winding is adopted. Therefore, the structure of the stator core can be designed as a multimodule spliced type, in which every stator tooth is used as a module with a separate winding coil. Every module can be manufactured separately and then assembled after winding each coil module. This process reduces the difficulty in winding, improves the coil space factor, and increases the output torque of the motor.

The stator core is spliced by 42 stator tooth modules, which are connected together by the core skeleton, as shown in Figure 7. A core retaining ring is set at each end of the core skeleton and connected to the core skeleton with a bolt to prevent the single stator tooth module from coming off. The assembly drawing of the entire stator structure is shown in Figure 8.



Figure 7. Connection diagram of single-tooth and core skeleton.



Figure 8. Multi-module spliced type stator structure.

Mechanical Structure of the Rotor

The mechanical structure of the rotor is relatively simple. It is mainly composed of the magnetic pole, rotor core, and wheel hub. The magnetic pole is attached to the inner surface of the rotor core, as shown in Figure 9. The threaded holes are machined at each end of the rotor core, which are used

to connect the wheel hub. The wheel hub is used to support the outer rotor. Therefore, the wheel hub is connected to the outer rotor with a bolt and to the fixed axis of the motor with a bearing, as shown in Figure 10.



Figure 9. Assembly drawing of magnetic poles and rotor core.



Figure 10. Assembly drawing of wheel hub. 1—bearing cap, 2—bearing, 3—end cap.

Integral Mechanical Structure of Motor

After the mechanical structures of all the parts are designed, the entire mechanical structure of the motor is generated, as shown in Figure 11.

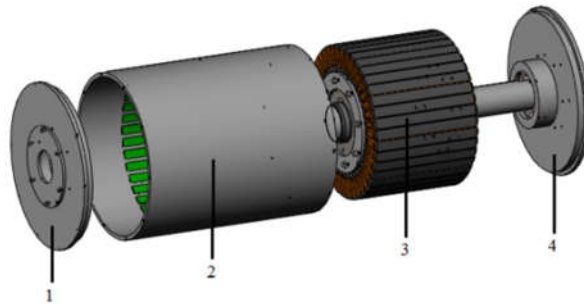


Figure 11. Assembly drawing of the whole motor structure. 1,4—wheel hub, 2—outer rotor, 3—stator.

3. Analysis of the Electromagnetic Field of the Outer-Rotor Direct-Drive Brushless DC Motor

3.1. Establishment of the Motor Model

The motor model is established using ANSYS Maxwell under the periodic boundary condition of the inner magnetic field distribution of the motor. As seen in Figure 12, half of the motor model is used in the simulation calculation to expedite the calculation.

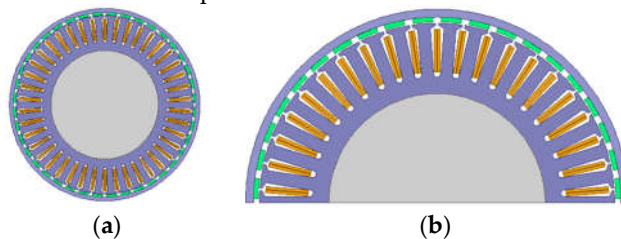


Figure 12. Whole model (a) and simplified model (b) of outer rotor brushless DC motor.

3.2. Analysis of the Static Magnetic Field of the Motor

The magnetic field that is constant even with a change in time is called a static magnetic field. When the motor is idle, the inner magnetic field generated by the magnetic pole is a static magnetic field. The magnetic flux distribution of the motor is obtained by analyzing the static magnetic field of the motor to evaluate the magnetic flux leakage of the motor and solve the magnetic flux leakage coefficient. The flux distribution of the motor is illustrated in Figure 13.

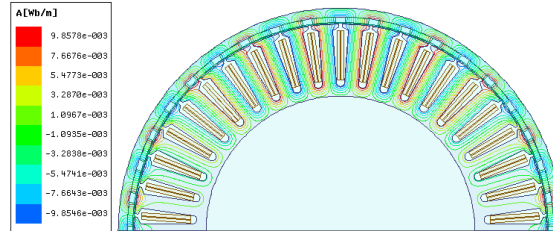


Figure 13. Flux lines distribution map of the brushless DC motor.

Figure 13 shows that the distribution of flux lines is nonuniform. The corresponding magnetic pole area of the stator teeth is unequal because of the fractional-slot windings. In addition, Figure 13 shows that the closed-loop of the few flux lines between the two magnetic poles is not completely through the stator teeth. Thus, magnetic flux leakage, which is quantified as the leakage coefficient, exists in the motor to some extent, but it is not serious [19]. Local amplification of the motor is performed to solve the pole-to-pole leakage coefficient of the motor, as shown in Figure 14.

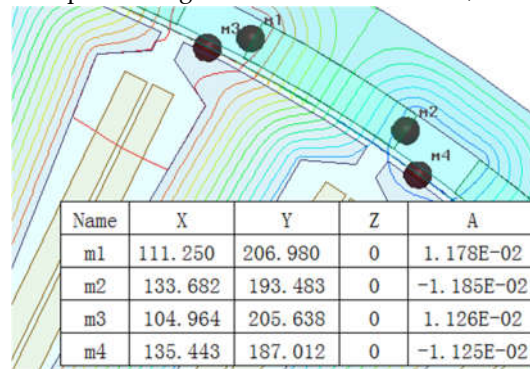


Figure 14. Partial enlarged drawing of flux lines.

The pole-to-pole leakage coefficient is calculated by taking a piece of permanent magnet to study and using Equation (9). The calculated result is 1.05, which shows that the pole-to-pole leakage coefficient is insignificant.

$$\sigma_1 = \frac{\varphi_m}{\varphi_\delta} = \frac{|m_1 - m_2| \cdot L_{ef}}{|m_3 - m_4| \cdot L_{ef}} = \frac{|m_1 - m_2|}{|m_3 - m_4|} \quad (9)$$

where φ_m is the total magnetic flux of permanent magnet (Wb), φ_δ is the main magnetic flux of the air gap (Wb), L_{ef} is the effective length of the core (mm), and m_1 , m_2 , m_3 , and m_4 are the vector magnetic potential values of the four points from Figure 15 (Wb/m).

The static magnetic flux density of the motor is shown in Figure 16, in which the different colors represent the different values of the magnetic flux density. Figure 15 indicates that no excessive saturation occurs in the motor and the maximum density of the magnetic flux exists in the stator tooth tip.

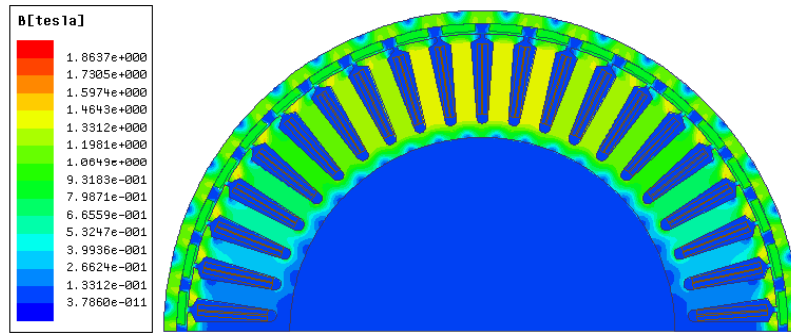


Figure 15. Inner flux density map of the motor under static condition.

The analysis of the air-gap magnetic field is the basis for the design and performance analysis of the brushless DC motor [20]. The air-gap flux density is mainly influenced by the pole thickness, air-gap length, and pole-arc coefficient. The air-gap flux density can be obtained by drawing the air-gap arc, which is a semicircular curve drawn between the inner diameter of the rotor and the outer diameter of the stator. Subsequently, the distribution curve of the air-gap flux density with respect to the circumferential direction can be obtained by post-processing, as shown in Figure 16.

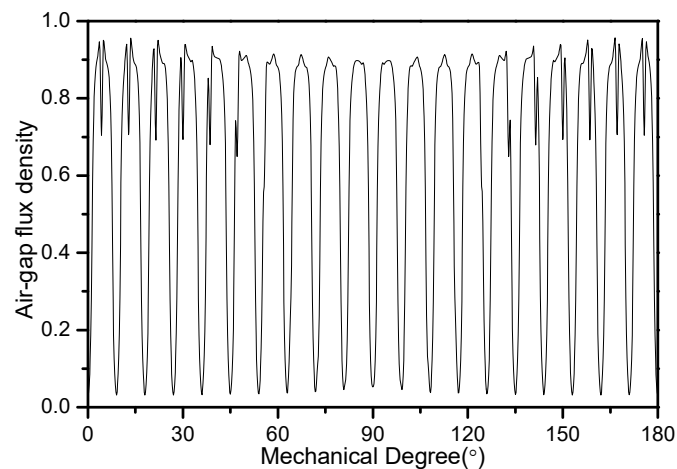


Figure 16. Air-gap flux density of the motor around the circle.

3.3. Analysis of the Transient Magnetic Field of the Motor

3.3.1. Analysis of the No-Load Transient Magnetic Field

When the motor is running in the no-load state, the current of the armature winding is minute, approximately zero. Under this condition, the magnetic field is produced by the permanent magnetic pole only, as in a static magnetic field. The difference is that the motor speed is a no-load speed rather than zero. In the no-load characteristic simulation of the motor, the excitation current of the winding should be set to zero, and the motor speed should be set to the no-load speed. The flux-linkage waveform and the back-EMF waveform of the three-phase windings can be obtained by post-processing, as shown in Figures 17 and 18, respectively.

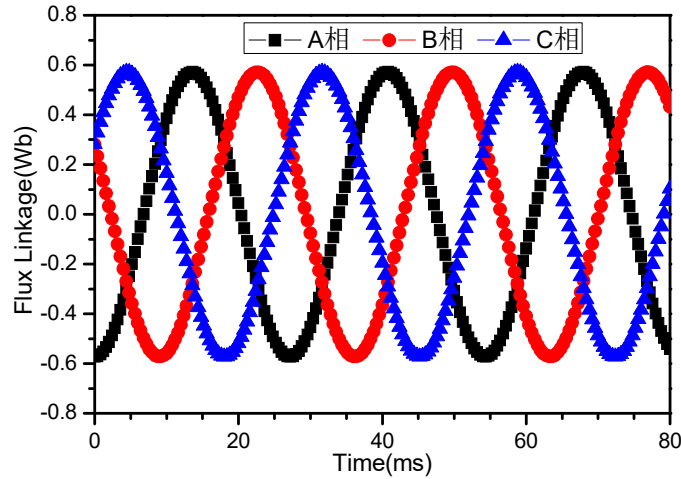


Figure 17. Waveform of three-phase flux linkage under no-load.

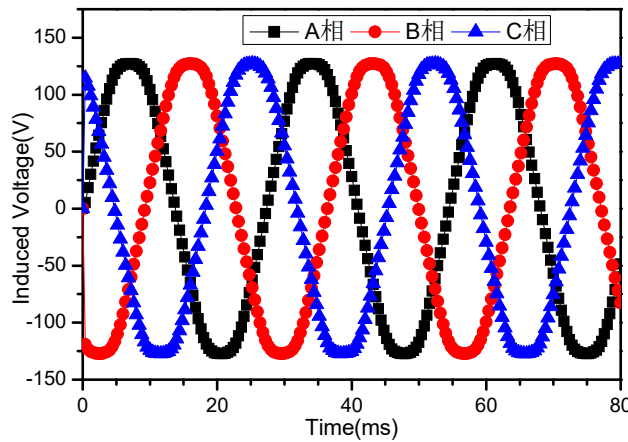


Figure 18. Waveform of three-phase back electromotive force under no-load.

3.3.2. Analysis of the Load Transient Magnetic Field

When the motor is running in the load state, the internal cloud of the magnetic flux density at the tooth tip is presented in the partially enlarged diagram of the motor under load operation (Figure 19). Figure 19 shows that the magnetic field distribution is similar to that of the no-load state. The internal magnetic flux density value is still located at the stator tooth tip, and the highest magnetic flux density is approximately 2 T. No saturation is evident, indicating that the motor design is reasonable.

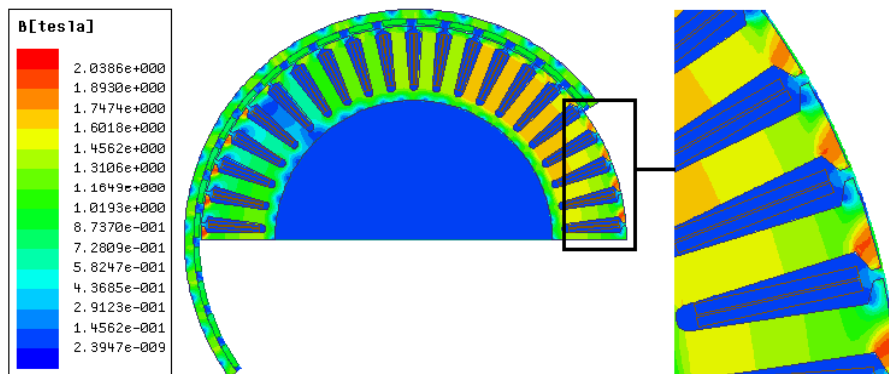
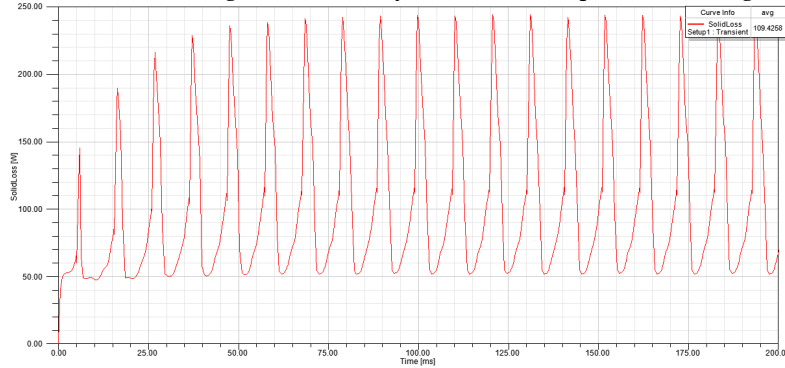
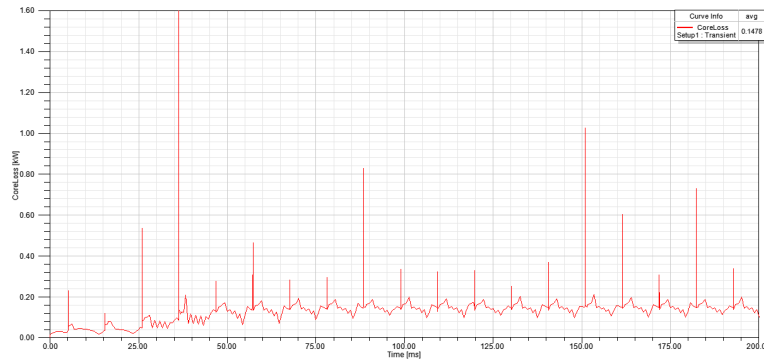


Figure 19. Inner flux density map of the motor under load.

3.4. Loss Analysis of the Motor

The loss of the motor running status can be divided into four categories: stator winding copper loss, core loss, eddy current loss of permanent magnet, and mechanical loss. The four types of loss vary with the stator current, the frequency of the main magnetic field, the motor speed, and the harmonic components of the stator current.

In this paper, finite element analysis is used to obtain the time domain curve of core loss and permanent magnet eddy current of the motor. As shown in Figures 20 and 21, the average value of core loss was 109 w, and the average value of eddy current loss of permanent magnet was 148 w.

**Figure 20.** Time domain curve of core loss.**Figure 21.** Time domain curve of eddy current loss of permanent magnet.

The calculation of copper loss is relatively simple. The calculation formula without considering current harmonic and skin effect is shown as follows [21]:

$$P_{cu} = mI_1^2R_s \quad (10)$$

where P_{cu} is the copper loss, m is the phase number, I_1 is the effective value of the phase current, and R_s is the average resistance of phase winding. The calculated copper loss is 3.32 kW.

4. Analysis of the Torque Ripple Characteristics of the Outer Rotor Direct-Drive Brushless DC Motor

4.1. Analysis of the Cogging Torque

A previous study [22] suggested that the fluctuation cycle of the cogging torque of a permanent-magnet motor is equal to the least common multiple of the pole number and the tooth-slot number. The pole number of the designed brushless DC motor is 40, and its slot number is 42; therefore, the

fluctuation cycle of the cogging torque is $360^\circ/420 = (6/7)^\circ$. The external circuit of the brushless DC motor is disconnected via ANSYS Maxwell, with the excitation source changed to the current source and the winding current set to zero. Subsequently, the speed of the motor is changed to $1^\circ/s$, and the simulation time is set to 3 s in the finite-element simulation. The output torque is the cogging torque of the motor, as shown in Figure 22. The value of the cogging torque is small, and its maximum value is approximately 2 N·m.

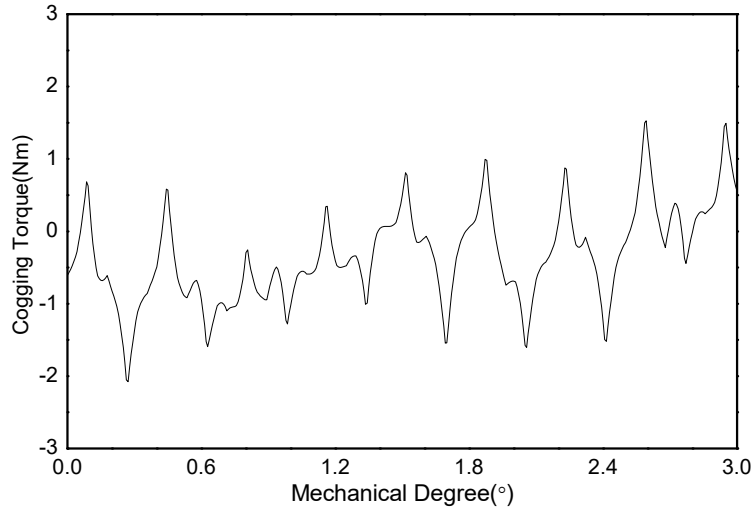


Figure 22. Waveform of the cogging torque.

4.2. Analysis of the Electromagnetic Torque

Electromagnetic torque refers to the torque generated by the interaction between the magnetic field of the permanent magnet and the stator winding current. From the point of view of electromechanical energy conversion and energy conservation, if the copper loss and iron loss are not considered, then the energy consumed by the armature winding is completely converted into the rotating mechanical energy of the rotor. The steady-state torque waveform of the brushless DC motor at the rated speed is shown in Figure 23. The steady-state torque is constantly fluctuating around 2 kN·m. The maximum torque value is 2.225 kN·m, and the minimum torque value is 1.865 kN·m. The torque pulses within the 36° mechanical angle are 12, and the pulsation cycle is 3° , which is not equal to the cogging torque cycle but equal to the commutation period of the brushless DC motor. The cogging torque has minimal effect on the steady-state torque, whereas the torque ripple is mainly caused by the current commutation. After the harmonics of the steady-state torque are analyzed, the harmonic torque amplitude in every order is determined (Figure 24).

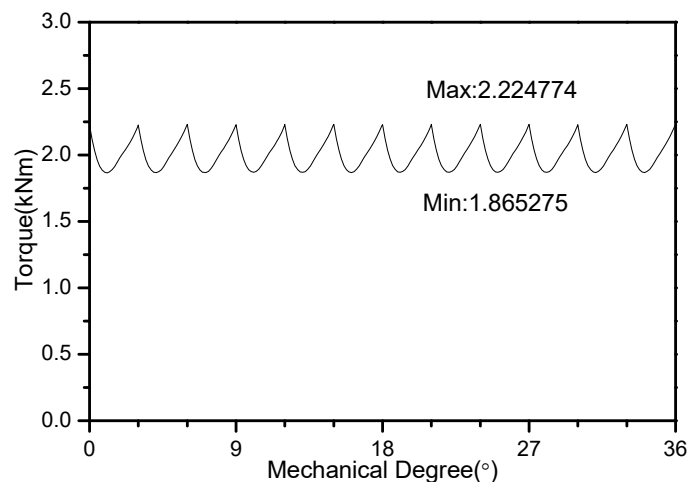


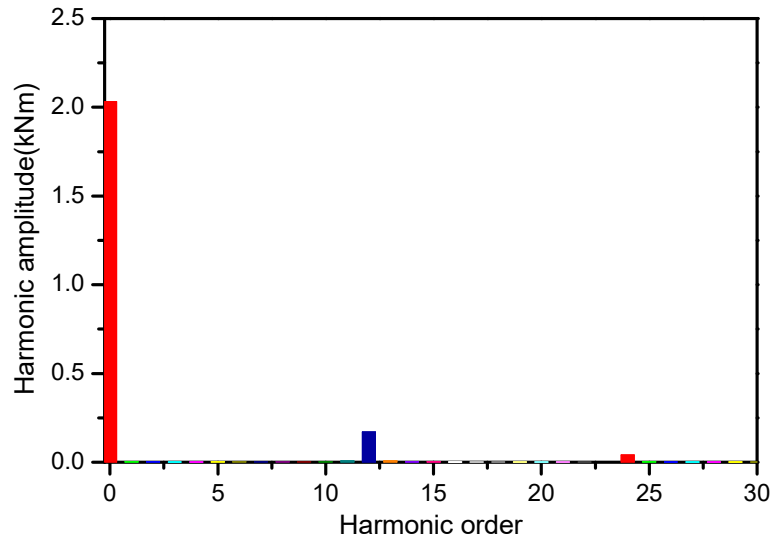
Figure 23. Steady-state torque of the brushless DC motor at rated speed.**Figure 24.** Harmonic analysis of steady-state torque.

Figure 24 shows that the DC component torque plays a prominent role in the steady-state torque. Furthermore, the harmonic torque in every order is caused by commutation and other reasons. The twelfth-order harmonic torque is dominant; thus, it is the main harmonic causing the torque ripple. If the twelfth-order harmonic torque of the motor can be eliminated, then the torque ripple of the motor can be significantly mitigated.

The average torque and the torque ripple factor of the motor can be calculated by Equations (11) and (12) to analyze the torque ripple condition of the motor. The greater the torque ripple factor of the motor is, the more serious the torque ripple of the motor is. The average torque is 2.045 kN·m, and the torque ripple factor is 17.58% (Figure 24).

$$T_{\text{avg}} = \frac{T_{\text{max}} + T_{\text{min}}}{2} \quad (11)$$

$$\text{TPF} = \frac{T_{\text{max}} - T_{\text{min}}}{T_{\text{avg}}} \times 100\% \quad (12)$$

where T_{max} is maximum torque (kN·m), T_{min} is minimum torque (kN·m), T_{avg} is average torque (kN·m), and TPF is torque ripple factor.

4.3. Reduction of the Torque Ripple of the Motor

The permanent-magnet brushless DC motor has many advantages, but there are also inevitable torque ripples, especially at lower speed. Usually, different methods are adopted to reduce the torque ripple, mainly from two aspects of the motor design and control. In terms of motor design, Chute of the stator or rotor skewed pole are commonly used, but the skewed pole makes the shape of the permanent magnet more special, so the process is complicated and not easy to manufacture. Chute stator also has certain problems; it not only increases the difficulty of the stator winding embedding, but also the low filling ratio. In order to solve the above problem, putting forward stator with two twisted modules based on the principle of chute, then the torque ripple of the motor can be reduced to allow the motor to run smoothly, and through to the stator unit separately controlled, the motor would have good fault tolerant performance; when a module is broken, another module is not affected, and can still continue to work. The 3D model of the outer rotor with the two twisted stators and the corresponding rotor is shown in Figures 25 and 26.

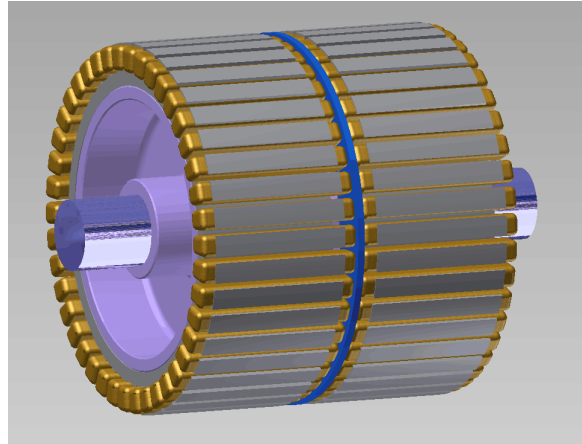


Figure 25. Diagram of the stator with two twisted modules.

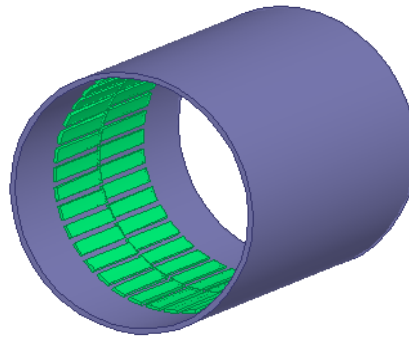


Figure 26. Diagram of the outer rotor.

The finite-element simulation of the two-dimensional magnetic field is based on the uniform distribution of the section magnetic field; the section magnetic field distribution between the two segments is different from that of the two twisted stators. The superposition method is employed to predict the total torque of the motor.

First, the half-length of the motor is used to conduct the finite-element simulation analysis of the magnetic field. Second, the stator of the motor is divided into two segments with the same length and the segment stators are placed axially skewed at 1.5°, equivalent to two units of motor. Then the total torque is equivalent to the superposition torque generated by the two units of motor, as shown in Figures 27 and 28.

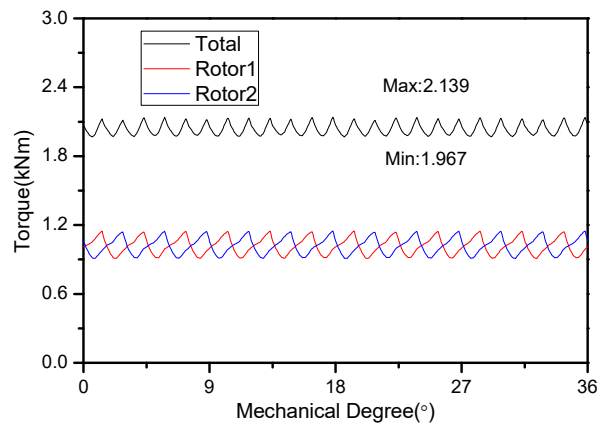


Figure 27. Torque waveforms of two units of motor and their total torque.

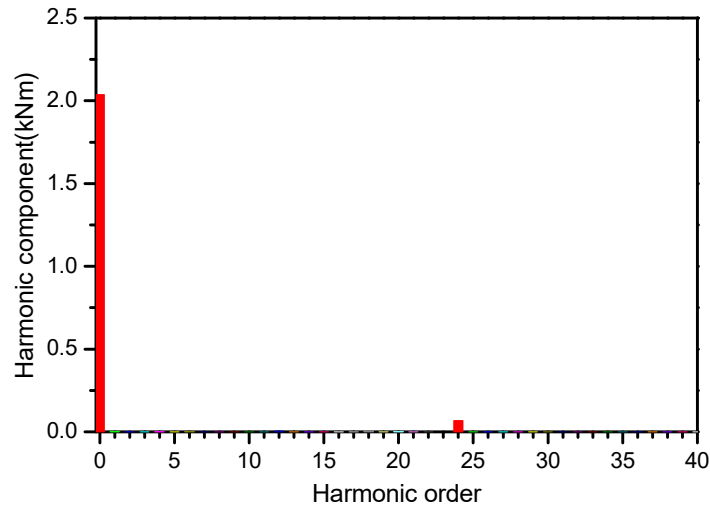


Figure 28. Harmonic analysis of the total.

Figure 27 indicates that the torque ripple amplitude is highly reduced compared with that in the original stator structure. The torque pulses within the 36° mechanical angle are 12, and the pulsation cycle is 1.5° . The pulsation frequency is twice that of the original one. The maximum and minimum values of the total torque are 2.139 kN·m and 1.967 kN·m, respectively. The average torque and the torque ripple factor calculated by Equations (4) and (5) are 2.053 kN·m and 8.4%, respectively. Compared with the torque in the original stator, the average torque is basically constant, and the torque ripple factor is remarkably reduced. This result indicates that the optimization method is effective in reducing the torque ripple. Figure 28 illustrates that the twelfth-order harmonic torque of the total torque has been offset compared with the original harmonic torque.

5. Conclusion

In consideration of the performance requirements for a middle or low speed direct-drive motor for an appointed electric vehicle, a direct-drive outer rotor brushless DC motor has been designed. It replaces the traditional centralized driving pattern of the electric vehicle. The main dimensions of the motor have been preliminarily calculated, and on this basis the air-gap length and the pole-arc coefficient, which are important parameters of the motor, have been optimized using the equivalent magnetic circuit method. The optimization of these parameters not only ensures the efficiency of the motor but also improves its operation reliability; the electromagnetic design scheme is finally determined, and the mechanical structure of the motor has been designed using the optimized parameters. The two-dimensional finite-element model of the motor has been established using ANSYS Maxwell, and the static magnetic field and transient magnetic field of the motor have been analyzed. The results show that the design of the motor is reasonable. The causes of the torque ripple have been investigated on the basis of steady-state torque, and current commutation is the main cause of the torque ripple. In order to decrease torque ripple, the stator structure of the motor has been optimized, and the results indicate that the torque ripple factor of the motor has decreased significantly from 17.58% to 8.4%.

Author Contributions: Data curation, W.M.; Investigation, X.S.; Methodology, L.Z.; Writing—original draft, Y.Y.

Funding: The work was financially supported by the Shanxi Science and Technology Development Plan 2014 (Industrial) Project 20140321008-04; Shanxi Province Scientific and Technological Achievements transformation guidance Project 201604D131028; and the Shanxi Province Graduate Excellent Innovation Project Fund under Grant No. 20133116.

Conflicts of Interest: The authors declare no conflict of interest.

References

- Jinghong, L. Drive System Design and Simulation Analysis for Hybrid Electric Vehicles. *J. Shanghai Dianji Univ.* **2007**, *1*, 33–35.
- Ruiqing, D. New energy vehicles development strategy research. *J. New Ind.* **2011**, *1*, 18–24.
- Lianqiao, T. The Full Text of China's 13th Five-Year Plan. Available online: <http://www.woc88.com/doc-12659458.html>. (accessed on 1 March 2018).
- Ningning, T. *Finite Element Modeling and Multi-Field Coupling Analysis of BLDC Wheel Motor*; Jilin University: Jilin, China, 2014.
- Shumei, C.; Junyun, S. The Research of the Direct-driven Wheel Motor Applied in Electric Vehicle. *Micromotors Servo Tech.* **2006**, *39*, 68–70.
- Xinmei, L. *Design and Research of the High-Power Density Permanent Magnet In-Wheel Motor Based on the Reluctance Torque*; Harbin Institute of Technology: Harbin, China, 2008.
- Tesla, M.S. *Automotive Observer*. **2018**, *1*, 25–25.
- Zhenpo, W.; Fengchun, S.; Peng, L. *The Electric Car Principle and Application Technology*; Mechanical industry press: Beijing, China, 2015.
- Ekram, S.; Mahajan, D.; Fazil, M.; Patwardhan, V.; Ravi, N. Design Optimization of Brushless Permanent Magnet Hub Motor Drive Using FEA. In Proceedings of the International Conference on Electrical Machines and Systems, Seoul, Korea, 8–11 October 2007; Volume 8, pp. 8–11.
- Gombert, B.; Fischer, R.; Heinrich, W. Wheel-Hub Motors Criteria of Construction and Vehicle Integration. *ATZelektronik Worldw.* **2010**, *5*, 4–10.
- Rix, A.J.; Kamper, M.J. Radial-Flux Permanent-Magnet Hub Drives: A Comparison Based on Stator and Rotor Topologies. *IEEE Trans. Ind. Electron.* **2012**, *59*, 2475–2483.
- Xiong, S. Motor drive technology research of the electric car. *Silicon Val.* **2014**, *21*, 41.
- Li, G.; Ojeda, J.; Hoang, E.; Gabsi, M.; Lecrivain, M. Thermal-electromagnetic analysis for driving cycles of embedded flux-switching permanent-magnet motors. *IEEE Trans. Veh. Technol.* **2012**, *61*, 140–151.
- Hejra, M.; Mansouri, A. Optimal Design of a Permanent Magnet Synchronous Motor: Application of In-Wheel Motor. In Proceedings of the 15th International Renewable Energy Congress IREC, Hammamet, Tunisia, 25–27 March 2014.
- Kock, A.; Groninger, M.; Mertens, A. Fault Tolerant Wheel Hub Drive with Integrated Converter for Electric Vehicle Applications. Proceedings of 2012 IEEE Vehicle Power and Propulsion Conference. Seoul, Korea, 2012.
- Tashakori, A.; Ektesabi, M. Fault diagnosis of in-wheel BLDC motor drive for electric vehicle application. 2013 IEEE Intelligent Vehicles Symposium, Gold Coast, QLD, Australia, 2013.
- Li, Y.; Wenjin, D. *Theory and Practice of Motor Design*; Tsinghua University Press: Beijing, China, 2013.
- Sumin, W. *The Study on the Optimization for the Structural Parameters of Permanent Magnet Synchronous Motor Based on Ansoft*; University of Electronic Science and Technology: Chengdu, China, 2014.
- Feng, Y.; Yang, K.; Gu, C. Design and optimization of external-rotor torque motor. In Proceedings of the 12th International Conference on Electrical Machines and Systems, Funabori, Tokyo, 15–18 November 2009; pp. 1–4.
- Yuejin, Z.; Chunjiang, L.; Guanzhen, T. Analytical Method for Air-Gap Main Magnetic Field Computation of Surface Mounted Permanent Magnet Torque Motors. *Trans. China Electrotech. Soc.* **2011**, *26*, 13–17.
- Lei, L. *The Study of Thermal Characteristics in Various Conditions and Cooling System of Permanent Magnet Synchronous Motor in Pure Electric Vehicle*; Hefei University of Technology: Chengdu, China, 2015.
- Zhu, Z.Q. Influence of Design Parameters on Cogging Torque in Permanent Magnet Machines. *IEEE Trans. Energy Convers.* **2000**, *15*, 407–412.

